analytical chemistry

pubs.acs.org/ac Article

Multifunctional Supramolecular Hydrogel Modulated Heterojunction Interface Carrier Transport Engineering Facilitates Sensitive Photoelectrochemical Immunosensing

Dongquan Leng, Zhen Yu, Jinjie Liu, Weihan Jin, Tingting Wu, Xiang Ren, Hongmin Ma, Dan Wu, Huangxian Ju, and Qin Wei*

Cite This: *Anal. Chem.* 2024, 96, 8814−8821 Read Online

ACCESS | Metrics & More | Article Recommendations | Supporting Information

ABSTRACT: Highly responsive interface of semiconductor nanophotoelectrochemical materials provides a broad development prospect for the identification of low-abundance cancer marker molecules. This work innovatively proposes an efficient blank $WO_3/SnIn_4S_8$ heterojunction interface formed by self-assembly on the working electrode for interface regulation and photoregulation. Different from the traditional biomolecular layered interface, a hydrogel layer containing manganese dioxide with a wide light absorption range is formed at the interface after an accurate response to external immune recognition. The formation of the hydrogel layer hinders the effective contact between the heterojunction interface and the electrolyte solution, and manganese dioxide in the hydrogel layer forms a strong competition between the light source and the substrate photoelectric material. The process effectively improves the carrier recombination efficiency at the interface, reduces the interface reaction kinetics and photoelectric conversion efficiency, and thus provides strong support for target identification. Taking advantage of the process, the resulting biosensors are being explored for sensitive detection of human epidermal growth factor receptor 2, with a limit of detection as low as 0.037 pg/mL. Also, this study contributes to the advancement of photoelectrochemical biosensing technology and opens up new avenues for the development of sensitive and accurate analytical tools in the field of bioanalysis.

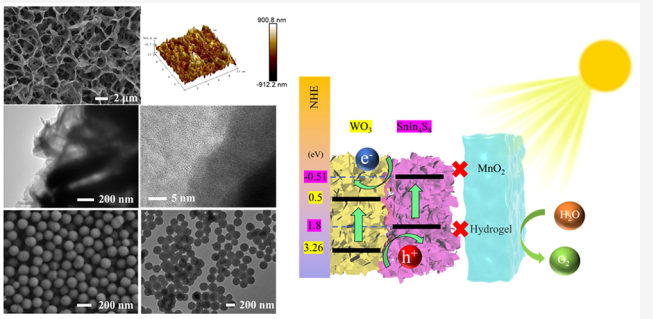

INTRODUCTION

In the field of biomedicine, photoelectrochemical (PEC) biosensors have expanded the frontier of biological diagnosis with their unique capabilities, which combine photochemical and biosensing technologies to detect and monitor biological events at the microbial, biomolecular, or cellular level.[1−8] Traditionally, photoelectrochemical biosensors have been employed to detect target analytes by utilizing interface reactions involving photoinduced electrons or excited species and biorecognition events.[9−11] These interface reactions, including charge transfer, chemical reactions, and immune reactions, facilitate signal transduction for the detection of target analytes.[12−15] The synergistic integration of these interface reactions with biosensing principles offers photoelectrochemical biosensors significant advantages such as high sensitivity, selectivity, and real-time monitoring.[16−18] Therefore, efficient use of a sensitive interface is the key to achieving high sensitivity detection. The split-type sensing strategy enhances the separation and electron transfer processes of photogenerated carriers significantly by exposing the active sites of semiconductor heterostructure materials to the electrolyte solution.[19,20] In this process, the exposed active sites provide an opportunity for signal amplification.

Hydrogel, a hydrophilic elastic polymer with a three-dimensional network, has garnered significant attention for its unique properties, including high water content and biocompatibility.[21−24] And it has found widespread application as a scaffolding material in tissue engineering,[25,26] regenerative medicine,[27,28] and drug delivery.[29,30] The unique properties of hydrogels are due to a variety of noncovalent driving forces, such as hydrogen bonding, van der Waals, $\pi-\pi$ stacking, and hydrophobic and electrostatic interactions,[31,32] but few examples have been reported in combination with multifunctional hydrogels in the field of photoelectrochemical sensing. Zhang et al.[33] used DNA hydrogels as blocking agents between photoelectric materials and influenced the blocking effect of hydrogels through the process of rolling circle amplification target recognition, thus changing the photocurrent signal. Zhao

Received: March 16, 2024
Revised: May 9, 2024
Accepted: May 10, 2024
Published: May 16, 2024

https://doi.org/10.1021/acs.analchem.4c01416
Anal. Chem. 2024, 96, 8814−8821

et al.[34] achieved sensitive detection of human IgG by generating hydrogels on the surface of PEC transistors by controlling release of Ca^{2+}. Supramolecular hydrogels composed of metal cations and low molecular weight anionic complexes adenosine 5′-monophosphate (AMP) are highly effective hindrance factors for carrier separation and diffusion on the surface of heterojunction materials, and the addition of manganese dioxide as a competitive light source during the formation of hydrogels would enhance the performance of photoelectrochemical immunosensing.

Before the surface carriers can be restricted to diffusion, there needs to be enough electron hole pairs within the heterojunction to be separated; that is, an efficient semiconductor is required.[35−37] When energized by photons, the internal bandgap structure can support the migration of electrons to the surface for the next step. WO_3 has a high bandgap energy (2.6−2.8 eV), and indium tin sulfide ($SnIn_4S_8$) is a new type of sulfide semiconductor material with good light absorption properties. This work innovatively proposes an efficient blank $WO_3/SnIn_4S_8$ heterojunction, which has good light absorption performance and wide wavelength response characteristics, and the matched band gradient structure can promote the separation of a photogenerated carrier and improve the photoelectric conversion efficiency. Different from the traditional biomolecular layered interface, a hydrogel layer containing manganese dioxide with a wide light absorption range is formed at the interface after an accurate response to external immune recognition. The formation of the hydrogel layer hinders the effective contact between the heterojunction interface and the electrolyte solution, and the manganese dioxide in the hydrogel layer forms a strong competition between the light source and the substrate photoelectric material. The process effectively improves the carrier recombination efficiency at the interface, reduces the interface reaction kinetics and photoelectric conversion efficiency, and thus provides a strong support for target identification.

EXPERIMENTAL SECTION

Reagents and Equipment. The experimental details (equipment, reagents, etc.) are placed in Supporting Information.

Preparation of WO_3. A modified synthesis method was used to prepare WO_3 nanoplate arrays.[9] A 0.23 g portion of $Na_2WO_4{\cdot}2H_2O$ was dissolved in 30 mL of deionized water, followed by the slow addition of 5 mL of 6 M hydrochloric acid. The mixture was stirred for 10 min. Next, 30 mL of 0.0537 M $(NH_4)_2C_2O_4$ solution was prepared and stirred for another 10 min. The resulting solution was then subjected to a 12 h hydrothermal reaction at 120 °C in a Teflon sealed autoclave with a volume of 50 mL, containing the solution and FTO substrate. The WO_3 precursor was washed three times with deionized water and ethanol. Finally, the precursor was annealed at 450 °C for 2 h, resulting in the successful formation of white nanosheets.

Preparation of $SnIn_4S_8$ and $WO_3/SnIn_4S_8$. $WO_3/SnIn_4S_8$ composite material was synthesized by in situ growth on the surface of WO_3 using the hydrothermal method. Initially, 30 mL of anhydrous ethanol was mixed with 0.2 mmol of $SnCl_4{\cdot}5H_2O$, 0.8 mmol of $InCl_3{\cdot}4H_2O$, and 2 mmol of thioacetamide. The resulting mixture was then magnetically stirred at room temperature for 20 min to ensure homogeneity. Subsequently, the homogeneous mixture was transferred to a Teflon sealed autoclave containing WO_3 glass plates and subjected to a reaction at 160 °C for 240 min. Finally, the FTO/WO_3/$SnIn_4S_8$ substrates were washed with ethanol, and the effective area of the loaded nanomaterials was 0.8 cm^2. $SnIn_4S_8$ was prepared without WO_3 glass plates under the same raw material and reaction conditions.

Preparation of Polydopamine NPs and GR-polydopamine NPs-Ab_2. Initially, dopamine hydrochloride (50 mg) and $FeCl_3{\cdot}6H_2O$ (8 mg) were dissolved in 150 mL of deionized water while subjected to stirring for 60 min under ambient conditions. Then, 20 mL of pH 8.4 Tris solution was added, and the mixture was stirred for additional 120 min. The resulting product was washed and dispersed in 5 mL of PBS. The obtained PDA NPs dispersion solution was added with 1 mL of Ab_2 (10 mg/mL) and 20 mg of glutathione reductase, and the mixture was oscillated at 4 °C for 5 h. The unbound protein molecules were then separated by centrifugation at 3000 r in a cryogenic centrifuge. Finally, the product was dispersed in 5 mL of PBS solution containing 10 mg of BSA and stored at 4 °C for later use.

Biosensor Fabrication and Detection Procedure. The preparation of the working electrode and the immune recognition process are illustrated in Scheme 1. The first

Scheme 1. Fabrication of Biosensor and Immune Recognition Process

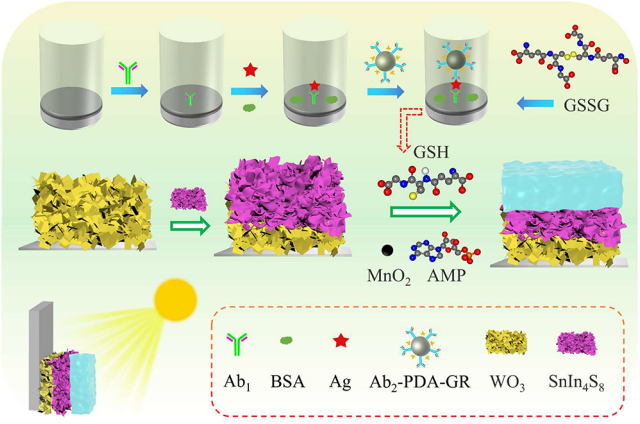

antibody was fixed in the microplate by physical adsorption, and 50 μL of Ab_1 with a concentration of 1 mg/mL was incubated at 4 °C for 10 h. Then bovine serum albumin, different concentrations of antigens, and GR-polydopamine NPs-Ab_2 complexes were added in sequence at 37 °C for incubation for 40 min. Each of these steps was cleaned using PBS (0.1 mol/L, pH = 7.4) solution. The 0.2 M GSSG was then added to the microplate for 25 min, and the solution was removed and mixed with manganese dioxide. The mixture was then dropped on the FTO/WO_3/$SnIn_4S_8$ electrode at the same time as the adenosine monophosphate solution (c_{AMP}:c_{NaOH} = 1:1.25). The electrode was rinsed and placed in an electrolytic cell containing PBS electrolyte for photochemical testing after the hydrogel formation.

RESULTS AND DISCUSSION

Characterization of Materials. The successful preparation of the materials during construction of the sensor was confirmed in terms of morphology and structure. The X-ray diffraction (XRD) characterization of WO_3, $SnIn_4S_8$, and the

https://doi.org/10.1021/acs.analchem.4c01416
Anal. Chem. 2024, 96, 8814−8821

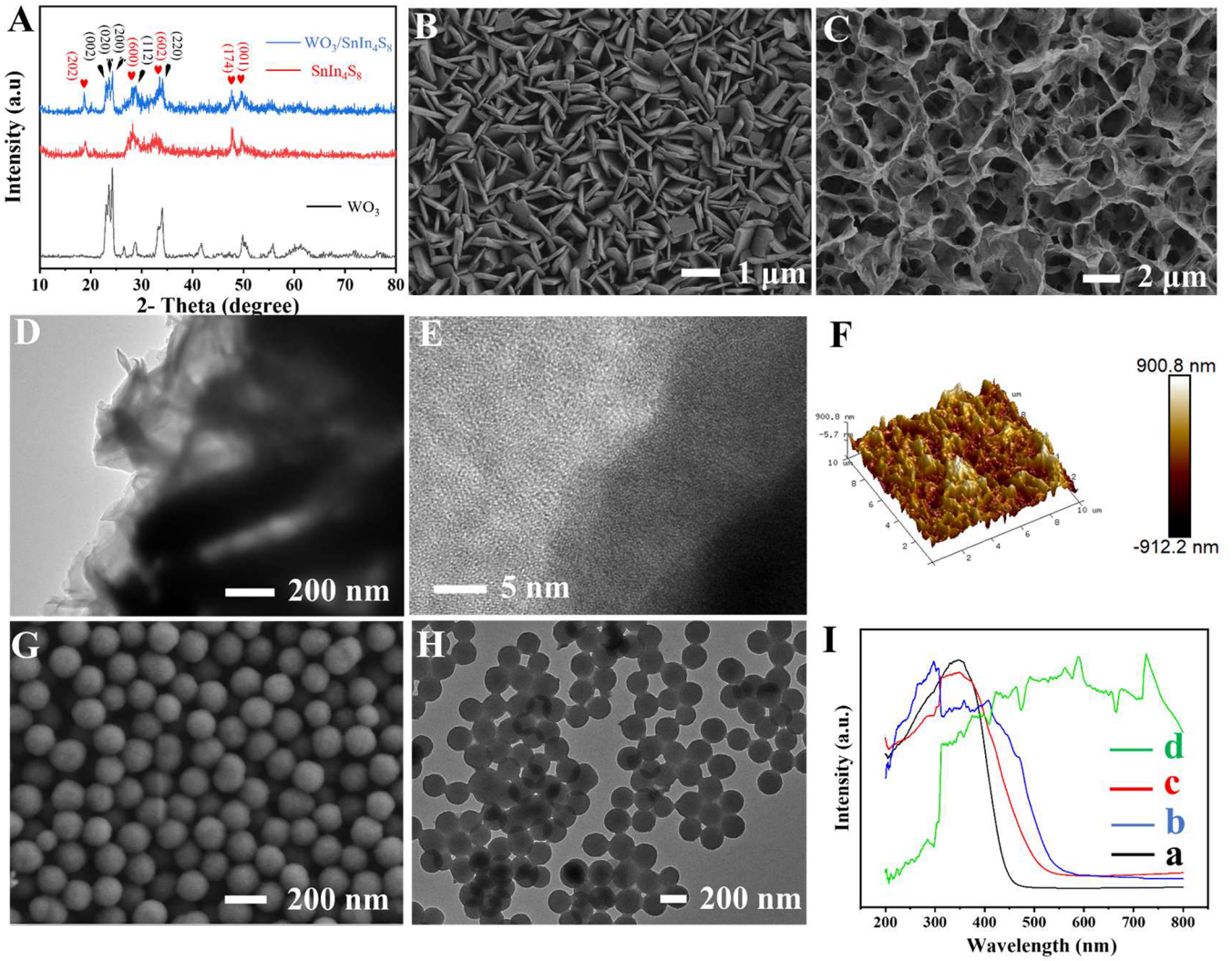

Figure 1. (A) XRD results of WO_3, $SnIn_4S_8$, and $WO_3/SnIn_4S_8$, SEM images of (B) WO_3 and (C) $WO_3/SnIn_4S_8$, (D, E) TEM images of $WO_3/SnIn_4S_8$, (F) AFM image of $WO_3/SnIn_4S_8$, (G, H) SEM and TEM images of PDA, and (I) DRS results of WO_3, $SnIn_4S_8$, $WO_3/SnIn_4S_8$, and MnO_2.

$WO_3/SnIn_4S_8$ composite structure shown in the Figure 1A demonstrates that the structure of the individual materials was consistent with the reported literature.[38] In the composite material, the diffraction peak at 23.14° (0 0 2), 23.64° (0 2 0), 24.37° (2 0 0), 28.87° (1 1 2), and 34.47° (2 2 0) corresponds to the characteristic peak of tungsten oxide material, and the diffraction peak at 19.18° (2 0 2), 28.23° (6 0 0), 32.86° (6 0 2), 47.94° (1 7 4), and 49.84° (0 0 1) corresponds to the characteristic peak of $SnIn_4S_8$. This result confirms the successful integration of the heterojunction composite material. The scanning electron microscopy (SEM) revealed that tungsten oxide was uniformly arranged in an array on the surface of the FTO glass in Figure 1B. Figures 1C and S1A illustrate the shape of petal-like films of $SnIn_4S_8$ completely covering the tungsten oxide surface. This configuration effectively absorbs light due to its loose structure, enabling substantial contact with the electrolyte solution for efficient charge transfer. Energy-dispersive spectroscopy (EDS) demonstrated the uniform distribution of elements W, O, Sn, In, and S on the FTO surface (Figure S2), indicating the successful fabrication of $SnIn_4S_8$ nanosheets on the WO_3 nanosheet arrays. Furthermore, this setup concurrently facilitates the formation of hydrogels on its surface. Further analysis using transmission electron microscopy (TEM, Figures 1D,E and S1B) showed that after the growth of $SnIn_4S_8$ on the oxide surface, the nanosheets array was completely enveloped, forming a tightly connected heterojunction state, which enhances the efficiency of interface electron transfer. In addition, atomic force microscopy (AFM) further demonstrated that the surface thickness of this structure was 1.8 μm. Figure 1G,H presents SEM and TEM characterization results of polydopamine microspheres, and it can be observed that the uniformly dispersed microspheres have a size of approximately 150 nm, which facilitates the labeling of antibodies and glutathione reductase. Figure 1I displays the UV−visible absorption spectra of WO_3, $SnIn_4S_8$, $WO_3/SnIn_4S_8$, and MnO_2. Compared with WO_3, $SnIn_4S_8$ exhibited enhanced absorbance. The formation of heterojunction $WO_3/SnIn_4S_8$ upon $SnIn_4S_8$ modification results in sensitized light absorption, while the absorbance range of MnO_2 covers that of WO_3 and $SnIn_4S_8$ in the visible light range, conferring MnO_2 with strong light harvesting ability over $WO_3/SnIn_4S_8$.

The X-ray photoelectron spectroscopy (XPS) of WO_3 and $SnIn_4S_8$ has been thoroughly analyzed and discussed. For WO_3, the XPS characterization reveals prominent peaks corresponding to the W 4f and O 1s orbitals in Figure 2A.

https://doi.org/10.1021/acs.analchem.4c01416
Anal. Chem. 2024, 96, 8814−8821

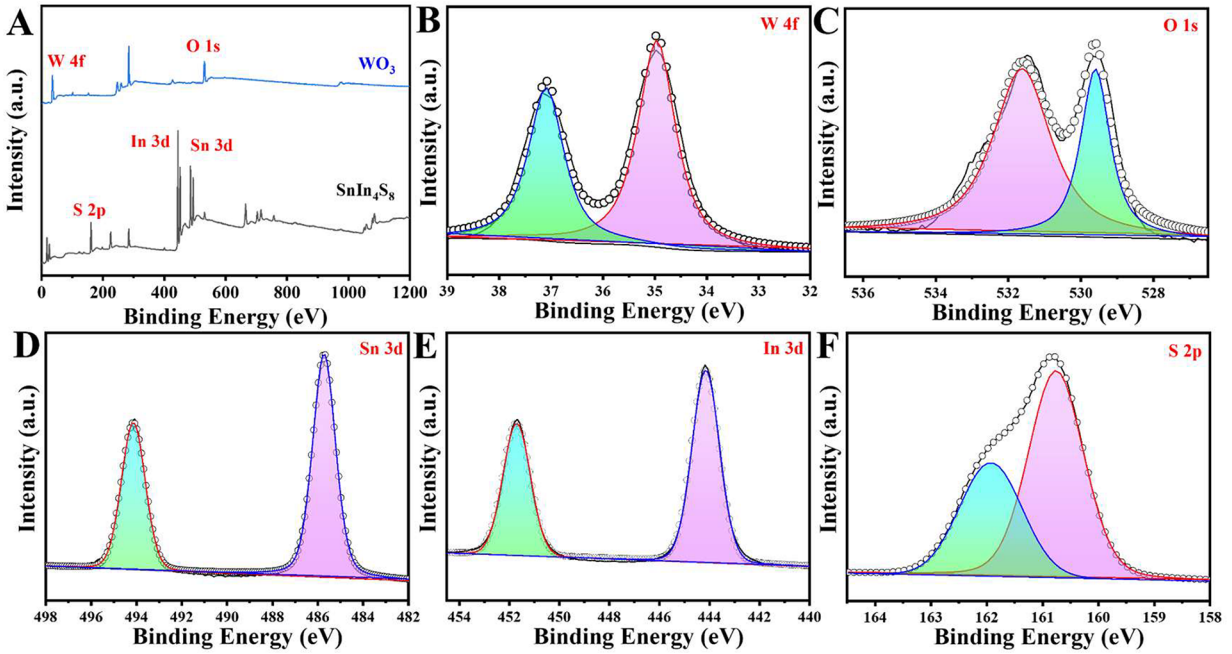

Figure 2. (A) XPS spectra of WO_3 and $SnIn_4S_8$. XPS spectra of (B) W 4f, (C) O 1s, (D) Sn 3d, (E) In 3d, and (F) S 2p.

The W 4f spectrum in Figure 2B exhibits characteristic peaks at binding energies of approximately 34.9 and 36.9 eV, representing the W $4f_{7/2}$ and W $4f_{5/2}$ levels, respectively. Additionally, the O 1s spectrum in Figure 2C shows a peak at a binding energy of around 531.6 and 529.6 eV, indicating the presence of OH^- and O^{2-} in the material. On the other hand, the XPS characterization of $SnIn_4S_8$ reveals prominent peaks corresponding to the Sn 3d, In 3d, and S 2p orbitals in Figure 2A. The characteristic peaks in the Sn 3d spectrum in Figure 2D are located at binding energies of 485.7 and 494.2 eV, representing the Sn $3d_{5/2}$ and Sn $3d_{3/2}$ levels, respectively. The binding energy peaks in the In 3d spectrum are observed at 444.1 and 451.7 eV in Figure 2E, corresponding to the In $3d_{5/2}$ and In $3d_{3/2}$ levels. Furthermore, the S 2p spectrum exhibits peaks at binding energies of approximately 160.7 and 161.9 eV, indicating the presence of sulfur in Figure 2F.

Possible Mechanisms of PEC Response. In order to investigate the mechanisms of photoconversion and analytical detection, UV−visible diffuse reflectance spectroscopy (DRS) and Mott−Schottky testing were employed to estimate the bandgap for inferring the diffusion pathways of photogenerated charge carriers and to understand the influence of MnO_2-doped hydrogel on this process. According to the diffuse reflectance spectroscopy spectra, the bandgaps for WO_3 and $SnIn_4S_8$ were calculated to be 2.76 and 2.31 eV in Figure S3, respectively. The flat band potentials of WO_3 and $SnIn_4S_8$ were found to be 0.60 eV and −0.41 eV relative to the normal hydrogen electrode (NHE), and 0.36 eV and −0.65 eV relative to the saturated calomel electrode (SCE) in Figure S4, respectively. For n-type semiconductors, the flat band potential is positive 0.1−0.3 eV relative to the conduction band potential; thus, the conduction bands of WO_3 and $SnIn_4S_8$ were calculated to be 0.50 eV and −0.51 eV, respectively. Using the bandgap calculation formula $E_g = E_{VB} - E_{CB}$, the valence band was calculated to be 3.26 eV for WO_3 and 1.80 eV for $SnIn_4S_8$. And WO_3 exhibits a large bandgap, while $SnIn_4S_8$ possesses a smaller bandgap. Upon illumination, photons excite electrons in both WO_3 and $SnIn_4S_8$, generating electron−hole pairs. Due to the bandgap alignment, these electron−hole pairs undergo charge separation, with the electrons accumulating in the conduction band of WO_3 and the holes migrating to the valence band of $SnIn_4S_8$ where they undergo charge exchange with the electrolyte solution, thus producing photocurrent and realizing the photoelectrochemical functionality in Figure 3. The supramolecular hydrogel

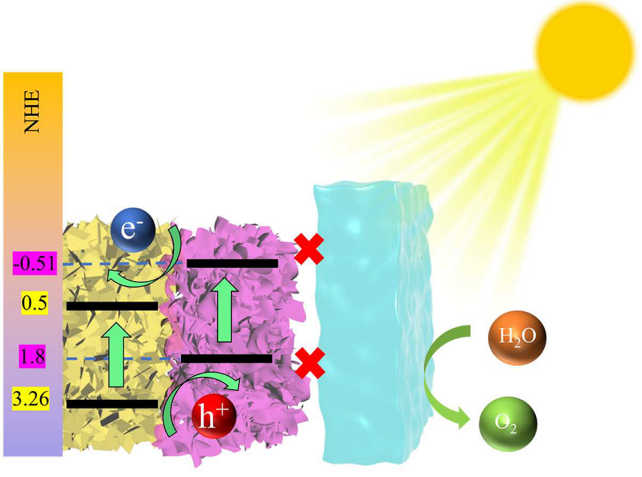

Figure 3. Mechanism of PEC and signal quenching.

exhibits quenching of the photocurrent response due to its weak conductivity and spatial hindrance effect on the diffusion and transport of charge carriers between the electrode and electrolyte solution. Meanwhile, the doping of manganese dioxide within the hydrogel competes strongly with the substrate material due to its broad spectral absorption range, resulting in synergistic quenching of the photocurrent response.

Biosensor Feasibility Analysis and Optimization. Each step of the biosensor construction process affects the performance of the sensor. This section describes the

https://doi.org/10.1021/acs.analchem.4c01416
Anal. Chem. 2024, 96, 8814−8821

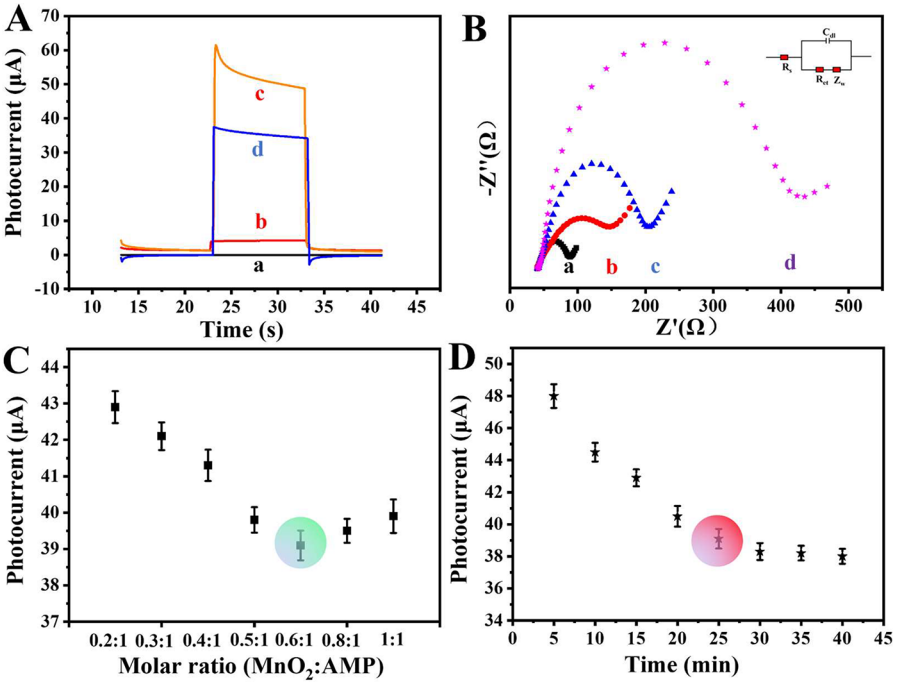

Figure 4. (A) PEC response in 0.1 M pH 7.4 PBS and (B) EIS in 5.0 mM $[Fe(CN)_6]^{3-/4-}$ containing 0.1 M KCl of (a) ITO, (b) ITO/WO_3, (c) ITO/WO_3/$SnIn_4S_8$, and (d) ITO/WO_3/$SnIn_4S_8$/hydrogel, (C) photocurrent response at different molar ratios of MnO_2:AMP in 0.1 M pH 7.4 PBS (c_{HER2} = 0.01 ng/mL), and (D) photocurrent response of different catalytic times in 0.1 M pH 7.4 PBS (c_{HER2} = 0.01 ng/mL).

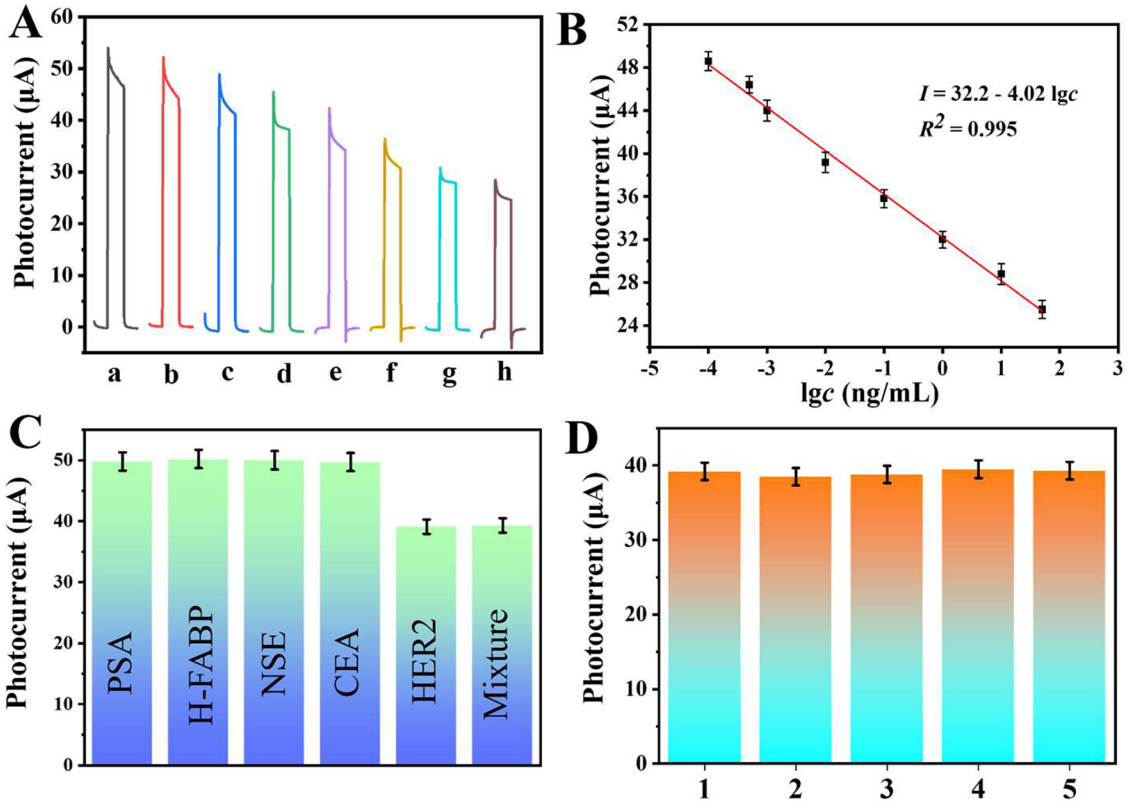

Figure 5. (A) Photocurrent response in 0.1 M pH 7.4 PBS (a–h), 0.0001, 0.0005, 0.001, 0.01, 0.1, 1, 10, and 50 ng/mL, (B) corresponding calibration curve of HER2 detection, (C) selectivity test (in 0.1 M pH 7.4 PBS, c = 0.01 ng/mL), and (D) reproducibility test (in 0.1 M pH 7.4 PBS, c = 0.01 ng/mL). Error bars = SD (n = 3).

performance of the sensor at different stages through photocurrent response and electrochemical impedance spectroscopy. The photocurrent response of fluorine-doped tin oxide conductive glass showed no response in the photocurrent response graph (Figure 4A). However, after the dense nanosheet array was grown on its surface using a hydrothermal

https://doi.org/10.1021/acs.analchem.4c01416
Anal. Chem. 2024, 96, 8814−8821

method, a weak photocurrent response was observed. Subsequently, with the in situ growth of $SnIn_4S_8$ thin film on the surface, a significant enhancement in the photocurrent response was achieved, attributed to the formation of a heterojunction. Additionally, when a MnO_2-doped hydrogel was formed on the photoanode surface, a distinct quenching of the photocurrent signal was observed when analyzing the analyte, using an antigen with a concentration of 0.1 ng/mL. Electrochemical impedance spectroscopy (Figure 4B) also proved this process, and impedance of the resulting hydrogel increased significantly due to weak conductivity and steric hindrance to electron diffusion.

The mixing ratio of manganese dioxide to adenosine monophosphate affects the formation of the hydrogel as well as the proportion of manganese dioxide, thus influencing the photocurrent response. Therefore, testing and optimization of these conditions were conducted. Using a target substance of 0.01 ng/mL as a reference, different mixing ratios (0.2:1, 0.3:1, 0.4:1, 0.5:1, 0.6:1, 0.8:1, 1:1) were adjusted and tested for their effect on the quenching of the photocurrent response. In Figure 4C, it can be observed that the hydrogel composite formed at a ratio of 0.6:1 exhibited the strongest influence on the photocurrent quenching process. The catalytic production of glutathione by glutathione reductase serves as a crucial link connecting the photoelectrode and the immunorecognition process, thus making it necessary to select an optimal catalysis duration. According to the results in Figure 4D, a catalysis duration of 25 min at room temperature was chosen as the optimal experimental condition.

HER2 Analysis. The concentration of human epidermal growth factor receptor-2 (HER2) in the human body is associated with the occurrence and progression of breast cancer tumors and can serve as an important clinical monitor and prognostic indicator. It also represents a crucial target for the selection of tumor-targeted therapeutic drugs. The split-type biosensor was used to detect varying concentrations (0.1 pg/mL to 50 ng/mL) of the standard target analyte HER2 under the optimized experimental conditions in Figure 5A. By plotting the PEC signal response against the logarithm of HER2 concentration, a calibration curve (Figure 5B) was obtained with the equation $I = 32.2 - 4.02 \log c$ (ng/mL), yielding a high correlation coefficient ($R^2 = 0.995$) and detection limit of 0.037 pg/mL.

Performance Analysis of Biosensor. The specificity and repeatability analysis are important performance indicators for biosensors,[39] and this part of the detection and results were determined. Specificity was evaluated by testing the interference of prostate specific antigen (PSA), heart fatty acid binding protein (H-FABP), neuron-specific enolase (NSE), and carcinoembryonic antigen (CEA) when present individually as well as in a mixed state with the target analyte on the photoelectrode. The results in Figure 5C indicate that the prepared biosensor exhibited good specificity. The repeatability analysis involved testing standard samples at the same concentration but in different batches of experimental conditions. The detected relative standard deviation was 3.6%, confirming the excellent repeatability of the biosensor, as shown in Figure 5D.

Serum Sample Analysis. To verify the applicability of the analytical method proposed in this study in actual samples, human serum samples were diluted 10-fold and analyzed using the standard addition method to assess the potential of the proposed biosensor.[40] The results, as shown in Table S1, indicated that when different concentrations of HER2 were added, the acceptable recovery rate ranged from 94.3% to 105.6%, with an RSD value of 2.4% to 4.3%. These data demonstrated the promising accuracy and practicality of the mentioned sensing strategy in clinical diagnosis.

CONCLUSION

This innovative work proposes a highly responsive WO_3/$SnIn_4S_8$ heterojunction interface biosensor for the identification of low-abundance cancer marker molecules. The self-assembled interface exhibits excellent sensitivity and selectivity, which is attributed to the efficient carrier recombination and photoelectric conversion processes. The formation of a hydrogel layer containing manganese dioxide at the interface following external immune recognition enhances the detection limit to 0.037 pg/mL for human epidermal growth factor receptor 2. This study significantly contributes to the advancement of photoelectrochemical biosensing technology and paves the way for the development of sensitive and accurate analytical tools in bioanalysis. The proposed strategy holds great potential for clinical diagnosis and opens new avenues for exploring similar applications in the field of cancer diagnostics.

ASSOCIATED CONTENT

Supporting Information

The Supporting Information is available free of charge at https://pubs.acs.org/doi/10.1021/acs.analchem.4c01416.

Materials and reagents, apparatus, elemental mapping of WO_3/$SnIn_4S_8$, UV−vis diffuse reflection spectra of WO_3 and $SnIn_4S_8$, bandgap diagram of WO_3 and $SnIn_4S_8$, and recovery experiments in human serum sample (PDF)

AUTHOR INFORMATION

Corresponding Author

Qin Wei − *Collaborative Innovation Center for Green Chemical Manufacturing and Accurate Detection, Key Laboratory of Interfacial Reaction & Sensing Analysis in Universities of Shandong, School of Chemistry and Chemical Engineering, University of Jinan, Jinan 250022, P. R. China; Department of Chemistry, Sungkyunkwan University, Suwon 16419, Republic of Korea;* orcid.org/0000-0002-3034-8046; Phone: +86 531 82767872; Email: sdjndxwq@163.com

Authors

Dongquan Leng − *Collaborative Innovation Center for Green Chemical Manufacturing and Accurate Detection, Key Laboratory of Interfacial Reaction & Sensing Analysis in Universities of Shandong, School of Chemistry and Chemical Engineering, University of Jinan, Jinan 250022, P. R. China*

Zhen Yu − *Collaborative Innovation Center for Green Chemical Manufacturing and Accurate Detection, Key Laboratory of Interfacial Reaction & Sensing Analysis in Universities of Shandong, School of Chemistry and Chemical Engineering, University of Jinan, Jinan 250022, P. R. China*

Jinjie Liu − *Collaborative Innovation Center for Green Chemical Manufacturing and Accurate Detection, Key Laboratory of Interfacial Reaction & Sensing Analysis in Universities of Shandong, School of Chemistry and Chemical Engineering, University of Jinan, Jinan 250022, P. R. China*

https://doi.org/10.1021/acs.analchem.4c01416
Anal. Chem. 2024, 96, 8814−8821

Weihan Jin − *Collaborative Innovation Center for Green Chemical Manufacturing and Accurate Detection, Key Laboratory of Interfacial Reaction & Sensing Analysis in Universities of Shandong, School of Chemistry and Chemical Engineering, University of Jinan, Jinan 250022, P. R. China*

Tingting Wu − *Collaborative Innovation Center for Green Chemical Manufacturing and Accurate Detection, Key Laboratory of Interfacial Reaction & Sensing Analysis in Universities of Shandong, School of Chemistry and Chemical Engineering, University of Jinan, Jinan 250022, P. R. China*

Xiang Ren − *Collaborative Innovation Center for Green Chemical Manufacturing and Accurate Detection, Key Laboratory of Interfacial Reaction & Sensing Analysis in Universities of Shandong, School of Chemistry and Chemical Engineering, University of Jinan, Jinan 250022, P. R. China;* orcid.org/0000-0002-4321-4282

Hongmin Ma − *Collaborative Innovation Center for Green Chemical Manufacturing and Accurate Detection, Key Laboratory of Interfacial Reaction & Sensing Analysis in Universities of Shandong, School of Chemistry and Chemical Engineering, University of Jinan, Jinan 250022, P. R. China;* orcid.org/0000-0002-7061-8944

Dan Wu − *Collaborative Innovation Center for Green Chemical Manufacturing and Accurate Detection, Key Laboratory of Interfacial Reaction & Sensing Analysis in Universities of Shandong, School of Chemistry and Chemical Engineering, University of Jinan, Jinan 250022, P. R. China;* orcid.org/0000-0002-8732-5988

Huangxian Ju − *Collaborative Innovation Center for Green Chemical Manufacturing and Accurate Detection, Key Laboratory of Interfacial Reaction & Sensing Analysis in Universities of Shandong, School of Chemistry and Chemical Engineering, University of Jinan, Jinan 250022, P. R. China; State Key Laboratory of Analytical Chemistry for Life Science, Department of Chemistry, Nanjing University, Nanjing 210023, P. R. China;* orcid.org/0000-0002-6741-5302

Complete contact information is available at: https://pubs.acs.org/10.1021/acs.analchem.4c01416

Notes

The authors declare no competing financial interest.

■ ACKNOWLEDGMENTS

This study was supported by the National Natural Science Foundation of China (Grants 22274062 and 22206056), the Shandong Provincial Natural Science Foundation (Grant ZR2022QB117), and Special Foundation for Taishan Scholar Professorship of Shandong Province. The authors thank Shiyanjia Lab (www.shiyanjia.com) for XPS analysis.

■ REFERENCES

(1) Bhachu, D. S.; Moniz, S. J. A.; Sathasivam, S.; Scanlon, D. O.; Walsh, A.; Bawaked, S. M.; Mokhtar, M.; Obaid, A. Y.; Parkin, I. P.; Tang, J.; et al. *Chem. Sci.* **2016**, *7* (8), 4832−4841.
(2) Ma, W.; Ma, H.; Peng, Y.-Y.; Tian, H.; Long, Y.-T. *Nat. Protoc.* **2019**, *14* (9), 2672−2690.
(3) Xiao, R.; Yu, H.; Liu, M.; Xu, W.; Qin, Y.; Tan, R.; Chen, Y.; Wen, J.; Peng, X.; Gu, W.; Zhu, C.; Hu, L. *Adv. Funct. Mater.* **2023**, *33* (46), 2304915.
(4) Kong, W.; Zhu, D.; Zhang, Y.; Luo, R.; Ma, J.; Lei, J.; Ju, H. *Angew. Chem., Int. Ed.* **2023**, *62* (33), No. e202308514.
(5) Leng, D.; Xu, R.; Ren, X.; Ma, H.; Liu, L.; Wei, Q.; Ju, H. *Chem. Eng. J.* **2023**, *469*, No. 143876.
(6) Qu, P.; Li, C.-J.; Hu, J.; Gao, G.; Lin, P.; Zhao, W.-W. *Anal. Chem.* **2023**, *95* (26), 9983−9989.
(7) Victorious, A.; Saha, S.; Pandey, R.; Soleymani, L. *Angew. Chem., Int. Ed.* **2021**, *60* (13), 7316−7322.
(8) Wang, H.-Y.; Xu, Y.-T.; Wang, B.; Yu, S.-Y.; Shi, X.-M.; Zhao, W.-W.; Jiang, D.; Chen, H.-Y.; Xu, J.-J. *Angew. Chem., Int. Ed.* **2022**, *61* (47), No. e202212752.
(9) Leng, D.; Ren, X.; Liu, L.; Zhang, D.; Zhang, N.; Ju, H.; Wei, Q. *Biosens. Bioelectron.* **2023**, *241*, No. 115710.
(10) Li, H.; Han, M.; Weng, X.; Zhang, Y.; Li, J. *ACS Nano* **2021**, *15* (1), 1710−1717.
(11) Abdi, G.; Alluhaibi, L.; Kowalewska, E.; Mazur, T.; Mech, K.; Podborska, A.; Sławek, A.; Tanaka, H.; Szaciłowski, K. *Coord. Chem. Rev.* **2023**, *487*, No. 215155.
(12) Huang, L.; Liang, Z.; Zhang, F.; Luo, H.; Liang, R.; Han, F.; Wu, Z.; Han, D.; Shen, J.; Niu, L. *Anal. Chem.* **2022**, *94* (46), 16246−16253.
(13) Niu, X.; Zhao, Y.; Wang, F.; Wu, J.; Qu, F.; Tan, W. *Anal. Chem.* **2021**, *93* (51), 17134−17140.
(14) Xu, J.; Zeng, R.; Huang, L.; Qiu, Z.; Tang, D. *Anal. Chem.* **2022**, *94* (32), 11441−11448.
(15) Yang, H.; Zhang, M.; Wang, L.; Yu, R.; Tu, W.; Wang, Z.; Wang, R.; Gao, H.; Dai, Z. *Anal. Chem.* **2021**, *93* (23), 8370−8378.
(16) Leng, D.; Zhao, J.; Ren, X.; Xu, R.; Liu, L.; Liu, X.; Li, Y.; Wei, Q. *Anal. Chem.* **2021**, *93* (30), 10712−10718.
(17) Gao, Y.; Zeng, Y.; Liu, X.; Tang, D. *Anal. Chem.* **2022**, *94* (11), 4859−4865.
(18) Dong, Q.; Xing, J.; Yuan, R.; Yuan, Y. *Anal. Chem.* **2023**, *95* (37), 13967−13974.
(19) Long, D.; Tu, Y.; Chai, Y.; Yuan, R. *Anal. Chem.* **2021**, *93* (38), 12995−13000.
(20) Wu, L.; Chen, S.-Y.; Fan, F.-J.; Zhuang, T.-T.; Dai, C.-M.; Yu, S.-H. *J. Am. Chem. Soc.* **2016**, *138* (17), 5576−5584.
(21) Hu, Y.; Shen, P.; Zeng, N.; Wang, L.; Yan, D.; Cui, L.; Yang, K.; Zhai, C. *ACS Appl. Mater. Interfaces* **2020**, *12* (37), 42285−42293.
(22) Mao, X.; Chen, G.; Wang, Z.; Zhang, Y.; Zhu, X.; Li, G. *Chem. Sci.* **2018**, *9* (4), 811−818.
(23) Zhao, L.; Li, L.; Yang, G.; Wei, B.; Ma, Y.; Qu, F. *Biosens. Bioelectron.* **2021**, *194*, 113597.
(24) Zhou, J.; Han, H.; Liu, J. *Nano Res.* **2022**, *15* (1), 71−84.
(25) Prince, E.; Kumacheva, E. *Nat. Rev, Mater.* **2019**, *4* (2), 99−115.
(26) Tang, J. D.; Mura, C.; Lampe, K. J. *J. Am. Chem. Soc.* **2019**, *141* (12), 4886−4899.
(27) Blache, U.; Ford, E. M.; Ha, B.; Rijns, L.; Chaudhuri, O.; Dankers, P. Y. W.; Kloxin, A. M.; Snedeker, J. G.; Gentleman, E. *Nat. Rev. Methods Primers* **2022**, *2* (1), 98.
(28) Pelloth, J. L.; Tran, P. A.; Walther, A.; Goldmann, A. S.; Frisch, H.; Truong, V. X.; Barner-Kowollik, C. *Adv. Mater.* **2021**, *33* (39), No. 2102184.
(29) Wang, X.; Ronsin, O.; Gravez, B.; Farman, N.; Baumberger, T.; Jaisser, F.; Coradin, T.; Hélary, C. *Adv. Sci.* **2021**, *8* (7), No. 2004213.
(30) Zhang, L.; Jean, S. R.; Ahmed, S.; Aldridge, P. M.; Li, X.; Fan, F.; Sargent, E. H.; Kelley, S. O. *Nat. Commun.* **2017**, *8* (1), 381.
(31) Yuk, H.; Lu, B.; Zhao, X. *Chem. Soc. Rev.* **2019**, *48* (6), 1642−1667.
(32) Kamata, H.; Kushiro, K.; Takai, M.; Chung, U.-i.; Sakai, T. *Angew. Chem., Int. Ed.* **2016**, *55* (32), 9282−9286.
(33) Liu, M.; Ma, W.; Zhou, Y.; Liu, B.; Zhang, X.; Zhang, S. *ACS Sensors* **2022**, *7* (10), 3153−3160.
(34) Hu, J.; Lu, M.-J.; Chen, F.-Z.; Jia, H.-M.; Zhou, H.; Li, K.; Zeng, X.; Zhao, W.-W.; Lin, P. *Adv. Funct. Mater.* **2022**, *32* (26), No. 2109046.
(35) Lu, L.; Zeng, R.; Lin, Q.; Huang, X.; Tang, D. *Anal. Chem.* **2023**, *95* (44), 16335−16342.
(36) Li, J.; Wang, H.; Liu, M.; Qin, Y.; Fang, Q.; Tan, R.; Hu, L.; Gu, W.; Zhu, C. *Anal. Chem.* **2023**, *95* (26), 10044−10051.

(37) Jin, L.; Cheng, F.; Li, H.; Xie, K. *Angew. Chem., Int. Ed.* **2020**, *59* (23), 8891−8895.
(38) Shen, C.-H.; Chen, Y.; Xu, X.-J.; Li, X.-Y.; Wen, X.-J.; Liu, Z.-T.; Xing, R.; Guo, H.; Fei, Z.-H. *J. Hazard. Mater.* **2021**, *416*, 126217.
(39) Huang, L.; Cai, G.; Zeng, R.; Yu, Z.; Tang, D. *Anal. Chem.* **2022**, *94* (26), 9487−9495.
(40) Gao, Y.; Li, M.; Zeng, Y.; Liu, X.; Tang, D. *Anal. Chem.* **2022**, *94* (39), 13582−13589.

https://doi.org/10.1021/acs.analchem.4c01416
Anal. Chem. 2024, 96, 8814−8821